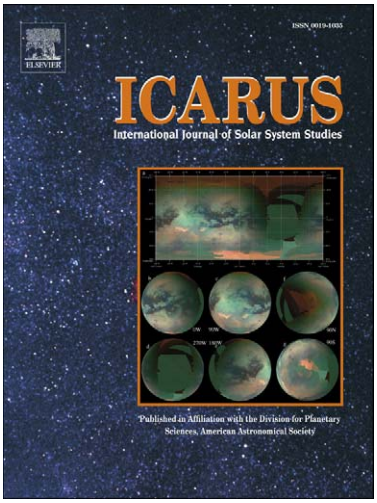

Investigation of water vapor on Mars with PFS/SW of Mars Express

M. Tschimmel, N.I. Ignatiev, D.V. Titov, E. Lellouch, T. Fouchet, M. Giuranna, V. Formisano

PII: S0019-1035(08)00074-2
DOI: 10.1016/j.icarus.2008.01.018
Reference: YICAR 8605

To appear in: *Icarus*

Received date: 3 July 2007
Revised date: 15 January 2008
Accepted date: 25 January 2008

Please cite this article as: M. Tschimmel, N.I. Ignatiev, D.V. Titov, E. Lellouch, T. Fouchet, M. Giuranna, V. Formisano, Investigation of water vapor on Mars with PFS/SW of Mars Express, *Icarus* (2008), doi: 10.1016/j.icarus.2008.01.018

Investigation of water vapor on Mars with PFS/SW of Mars Express

Tschimmel, M. [a], Ignatiev, N.I. [b], Titov, D.V. [a,b], Lellouch, E. [c], Fouchet, T. [c,d], Giuranna, M. [e], Formisano, V. [e]

[a] *Max Planck Institute for Solar System Research, 37191 Katlenburg-Lindau, Germany*

[b] *Space Research Institute (IKI RAN), Moscow 117997, Russia*

[c] *Observatoire de Paris, LESIA, Meudon 92195, France*

[d] *Université Pierre et Marie Curie - Paris 6, UMR 8109, Paris 75005, France*

[e] *Istituto di Fisica dello Spazio Interplanetario INAF-IFSI, 00133 Rome,Italy*

Number of pages: 51

Number of figures: 15

Preprint submitted to Icarus *27 February 2008*

Proposed Running Head:

Mars water cycle from PFS/SW observations (Mars Express)

Please send Editorial Correspondence to:

Dmitri V. Titov

Max-Planck-Institut für Sonnensystemforschung

Max-Planck-Str. 2

37191 Katlenburg-Lindau

Germany

Email: titov@mps.mpg.de

Phone: +49-5556-979-212

Fax.: +49-5556-979-240

ABSTRACT

New insight into the seasonal, diurnal and spatial distribution of water vapor on Mars has been obtained from analyzing the spectra of the short-wavelength channel (SW) of the Planetary Fourier Spectrometer (PFS) onboard Mars Express. The processed dataset, recorded between January 2004 and April 2005, covers the seasons from L_S=331° of Mars Year 26 to L_S=196° of the following year. In this period the mean column density around vernal equinox was 8.2 pr. µm. The maximum values during northern summer were about 65 pr. µm, located around 75°N latitude with a longitudinally inhomogeneous distribution. Regarding the atmospheric transport, the majority of polar water vapor remains in the north polar region while only about a quarter is transported southward. Geographically there are two water vapor maxima visible, over Arabia Terra and the Tharsis plateau, that are most likely caused both by atmosphere – ground interaction and by atmospheric circulation. A comparison with other instruments generally shows a good agreement, only the SPICAM results are systematically lower. Compared to the results from the PFS long-wavelength channel the results of this work are slightly higher. A strong discrepancy is visible northward of about 50°N during the northern summer that is possibly explained by a non-uniform vertical H_2O mixing. In particular, a confinement of the water to the lower few kilometers yields a much better agreement between the retrieved column densities of the two PFS channels.

Keywords: Mars ; Mars, atmosphere ; abundances, atmospheres ; atmospheres, structure ; infrared observations

1 Introduction

In the history of the exploration of Mars the question of water vapor was always of greatest interest because it is the most variable trace gas and involved in a number of processes in the martian atmosphere. Following initial ground-based observations in the early 1960's (Spinrad et al., 1963) more thorough investigations have become feasible with the progress of technology. Regarding the seasonal evolution of water vapor the first groundbreaking dataset was provided by the MAWD spectrometer onboard *Viking 1* using the 1.38 µm band. The main result from this experiment was the coverage of the entire seasonal cycle on Mars showing variations between a few up to 100 pr. µm. Based on this an exchange of vapor with surface reservoirs, namely the permanent and seasonal polar caps and the regolith, was suggested, as well as a net transport from north to south by global circulation (Jakosky and Farmer, 1982). Moreover, a recent reanalysis of the MAWD data stressed the importance of light scattering of aerosols on the retrieved water amount, especially in the near infrared range for observation geometries with high airmasses (Fedorova et al., 2004). In particular, the true water amount during the southern summer is masked by the dusty atmosphere demanding a correction of the retrievals when the airmass is higher than three.

In the late 1980's and the 1990's new spacecraft observations became available. First the ISM spectrometer on *Phobos 2* detected an average column density of 9±3 pr. µm in the south and 12±3 pr. µm in the north (Rosenqvist et al., 1992). Another *Phobos 2* instrument, Auguste, could provide an independent detection of 10 pr. µm of water with a mixing ratio of 150 ppm until an altitude of 12 km decreasing towards 3 ppm at 40 km (Krasnopol'skii et al., 1991). All

these observations were taking place around L_S=10°. In 1997 the camera of the *Pathfinder* lander photometrically detected a column density of 6±4 pr. µm in the Ares Vallis at L_S=150° but, more important, a confinement of the water vapor to the lower 1–3 km above the surface (Titov et al., 1999).

Between 1999 and August 2004 the Thermal Emission Spectrometer (TES) onboard *Mars Global Surveyor* recorded spectra covering the water bands between 20 and 45 µm. The large dataset covers more than two martian years at constantly 14:00 hours local time (Smith, 2004). However, after a reanalysis of the spectra taken in the lower resolution mode the results had to be corrected downwards by up to 30% (Smith, 2006). The complete seasonal coverage includes three northern summer maxima that showed a maximum column density of 55–65 pr. µm in MY 24, 60–70 pr. µm in MY 25 and 65–80 pr. µm in MY 26. These values are taken from the improved TES database (M. Smith, private communication).

In parallel to spacecraft observations water vapor was sounded with ground-based instruments at 0.82 µm. For information about the seasonal and inter-annual trends the large dataset by Sprague et al. (1996) allowed a comparison of two martian years during northern summer and showed a variation of up to a factor of 3 between the two years. Although the general shape of the seasonal cycle was repeated quite well, only 36.4 pr. µm were detected at 71.2°N during L_S=100°. Around the opposition of 1997 both for L_S=18.0–78.4° and L_S=113.7–146.4° the water was latitudinally and longitudinally distributed in an inhomogeneous way but generally consistent with the previously observed seasonal behavior. The maximum detected amounts were 40–45 pr. µm at latitudes between about 60–80°N both before and after the summer solstice (Sprague et al., 2003). At the same time of TES operations in MY 24 Sprague

et al. (2001) found 43–76 pr. µm at 75°N during L_S=105–115° and 9–17 pr. µm at 80°N around L_S=150–160°. Recently Sprague et al. (2006) reported so far unpublished results from the years 1998–1999. There the seasonal coverage of MY 24 is extended and stretches from L_S=34° to L_S=249°. The retrieved column densities vary generally between about 3 pr. µm and almost 25 pr. µm for the L_S outside the northern summer. Additionally, an intercomparison of results for different martian years shows MY 24 to be wetter than MY 22 and MY 23.

Since January 2004 Europe is contributing to the exploration of Mars with its own orbiter *Mars Express*. All three onboard spectrometers are able to sound the atmosphere for water. Encrenaz et al. (2005) and Melchiorri et al. (2007) published H_2O measurements of the OMEGA spectrometer that covers the 2.6 µm band and Fedorova et al. (2006) published the ones of the SPICAM instrument using the 1.38 µm band. Of the large spectral range covered by the Planetary Fourier Spectrometer (PFS) the results of the long-wavelength channel were presented by Fouchet et al. (2007) while the focus of this work is the water retrieval from the 2.6 µm band. The PFS instrument and the retrieval technique are described in the following two chapters while chapters 4 and 5 contain the results and the conclusions.

2 The Planetary Fourier Spectrometer: experiment and observations

The Planetary Fourier Spectrometer (PFS) onboard *Mars Express* was specifically designed for atmospheric sounding and is described in detail by Formisano et al. (2004) and Formisano et al. (2005). Only issues that are

relevant for this work are described in the following. PFS is a double pendulum Fourier spectrometer that detects infrared radiation simultaneously in two channels. The long-wavelength channel (LW) covers the thermal radiation of Mars between 5 and 40 µm (250–2000 cm^{-1}) and the short-wavelength channel (SW) is sensitive mainly to reflected sunlight in the range of 1.2 to 5.8 µm (1700–8200 cm^{-1}). The PFS/SW field of view of 1.6° provides a nadir SW footprint of about 8–80 km for a single spectrum, depending on the spacecraft altitude. The spectral response function of the instrument has a FWHM of 2.04 cm^{-1} with Hamming apodization and a spectral sampling step of 1.02 cm^{-1}. Apodized spectra were used for this work because of their noise reduction advantage and the decrease of the overshooting effect in the red wing that is typical for the PFS instrumental function. The operations during the science phase of each orbit generally start and end with taking – in most cases – 31 calibration measurements. Around the pericenter pass on average between 200 and 300 spectra are recorded depending on operational and orbital constraints.

Regarding the in-flight performance, there are three causes for instrumental uncertainties that have to be taken into account: problems with radiometric calibrations, random noise due to the detector and AD converter and the influence of spacecraft vibrations. The apparent loss of the optical alignment of the internal calibration lamp during launch makes the absolute radiative calibration of the spectra a complex task. In addition, the vibrations of the spacecraft seriously affect the spectrum at wavenumbers higher than 4200 cm^{-1}. Finally, the instrumental noise may alter the effective depth of the water absorption lines, leading to errors in the estimations of the vapor contents. To mediate all these problems the following measures were taken for the H_2O retrieval:

the averaging of spectra to reduce the noise and thus improve the signal-to-noise ratio (S/N) and the use of relative band depths, meaning the ratio of the band depth to the continuum, in order to be independent of the absolute calibration. As inferred by Comolli and Saggin (2005) and recently confirmed by Giuranna et al. (2007) the spacecraft vibrations affect only the level of the continuum leaving unaltered the relative depth of the atmospheric absorption lines. Details on the spectral and radiometric calibration procedures, as well as the in-flight performance and the effects of the external perturbations can be found in Giuranna et al. (2005). In that publication the noise equivalent radiance (NER) is reported to be about 0.02 erg $s^{-1}\,cm^{-2}\,sr^{-1}/cm^{-1}$ in the range of the 2.6 µm H_2O band. This value must be divided by a factor of almost 4 due to the averaging of spectra (see below). With the given assumption the S/N for the averaged spectra used in this work ranges from a minimum of about 20 (orbit 930, average of spectra 40 to 54) to a maximum of 335 (orbit 1345, average of spectra 13 to 27), with a mean value of S/N=115.

The PFS/SW dataset covers a bit more than half a martian year from L_S=331° of MY 26 (orbit 10) to L_S=195° of MY 27 (orbit 1609). The counting of martian years MY was defined by Clancy et al. (2000). The southern summer is not covered due to the activation of the MARSIS radar in May 2005 and a problem with the pendulum motor in the following months. Now for the creation of a single mean spectrum, which is later called datapoint, several measurements are averaged. The optimum averaging number was chosen to be 15 because of the reasonable compromise between an enhancement of S/N and the maintenance of good spatial resolution. So the footprint of a datapoint on the surface is about 0.8° to 2° in latitude or 50 to 120 km. For a single orbit this sliding window of 15 is shifted over all the observations as long as they have

a low enough airmass (generally 3.1, in special cases 3.7). In between there is a step of 4, i.e. average spectra are constructed from observations 1–15, 5–19, 9–23, ... and so on. All in all, for the presented work 21 214 datapoints with good quality were created whose distribution in local solar time and season is displayed in Fig. 1.

3 Retrieval procedure

Although PFS covers a large wavelength range with several water absorption bands only the 2.6 µm band was used because it is the strongest band and not affected by the spacecraft vibrations, too. The bands of the long-wavelength channel were independently analyzed by Fouchet et al. (2007) and these LW results are valuable for intercomparisons. For the aim of retrieving the H_2O column density for a datapoint (average of 15 spectra) the following procedure was developed:

(1) extraction of a vertical temperature and pressure profile from the European Mars Climate Database[1] (EMCD, version 4.1)
(2) line-by-line calculation of monochromatic opacities both for CO_2 and H_2O under consideration of the water saturation level
(3) multiplication of the created transmittance spectrum with the solar spectrum and convolution with the PFS instrumental function
(4) division by a specific continuum (normalization), both of the synthetic spectrum and the averaged PFS spectrum

[1] The original model is described by Lewis et al. (1999) and Forget et al. (1999) while the improvements of the used version are described by Forget et al. (2006).

(5) finding the H_2O mixing ratio (below the saturation level) in a fitting loop and a corresponding correction of the PFS continuum.

In the sections below these steps will be described in greater detail. Please note that dust scattering has not been incorporated in the procedure because the observations were taken mainly in the aphelion season with little dust activity and the 2.6 µm band is less sensitive to dust than the near-infrared bands. For those bands both Fedorova et al. (2004) (using SPICAM at 1.38 µm) and Sprague et al. (2006) (using groundbased observations at 0.82 µm) concluded that the airmass must be in the order of 4 to 6 to cause a measurable effect on the H_2O results. For this work all spectra with airmasses higher than 3.7 were excluded which should permit the neglection of dust scattering assuming that the dust is evenly distributed with a low optical depth. In addition, the wavenumber sampling of the measured PFS spectrum can be slightly shifted which requires a fine-tuning of the spectral grid before the start of the actual retrieval. The exact procedure using the laser diode temperature (cf. Giuranna et al. (2005)) as tuning parameter is described in greater detail in Tschimmel (2007).

3.1 Vertical atmospheric profiles

Before the creation of a synthetic spectrum the geometry information of the individual spectra (latitude, longitude, L_S and local time) are binned to mean values. These values are used to calculate the surface altitude from the MOLA $1/4^\circ \times 1/4^\circ$ database and to provide input for the EMCD. For the given coordinates this global circulation model yields an interpolated temperature and pressure profile with – in our case – 56 defined layers. The vertical resolution

of the profile increases from the upper atmosphere with 4 km resolution in 120 km altitude towards the surface where the resolution is 5 m. This profile naturally determines the H_2O saturation pressure p_S over ice (given in [Pa]) that was calculated following the recent measurements of Mauersberger and Krankowsky (2003) for low temperatures T [K]:

$$\begin{aligned} 169\,\mathrm{K} \leq T \leq 273.15\,\mathrm{K}: \quad & \log p_S = -\frac{2663.5 \pm 0.8}{T} + (12.537 \pm 0.011) \\ 164.5\,\mathrm{K} \leq T < 169\,\mathrm{K}: \quad & \log p_S = -\frac{3059 \pm 26}{T} + (14.88 \pm 0.15) \end{aligned} \tag{1}$$

3.2 The synthetic spectrum

To calculate the monochromatic transmittance spectrum effectively Titov and Haus (1997) developed a fast technique for transmittance calculations which was specifically refined for the application with PFS (Haus and Titov, 2000). The absorption coefficients at a wavenumber ν can be calculated rapidly for given atmospheric conditions with the use of a pre-calculated look-up matrix. This matrix has to be computed only once with a line-by-line code and includes a set of pressure-independent absorption coefficients. Specifically for this work the calculated spectral stepsize is with $0.01\,\mathrm{cm}^{-1}$ the highest in the line centers decreasing towards the wings. The calculations for an individual wavenumber were performed until a cutoff distance of $50\,\mathrm{cm}^{-1}$ to the red and blue side. Altogether this sums up to 55 710 wavenumber steps between $3700\,\mathrm{cm}^{-1}$ and $4100\,\mathrm{cm}^{-1}$. The line strengths and widths for the relevant gases H_2O and CO_2 were taken from the HITRAN 2004 database (Rothman et al., 2005). Because the spectral line database is created for the terrestrial atmosphere, the correction for CO_2-dominated air is done with a line broadening parameter. For this work the line widths were corrected according to the values calculated by

Gamache et al. (1995). However, one has to keep in mind that the broadening factors are different from line to line and can vary between 0.9 and 1.9 which leads to a large uncertainty in the retrieval.

In the next step the transmittance spectrum is calculated under consideration of the given airmass and the mixing ratio that is the tuning parameter in the retrieval algorithm. Moreover, with the presence of a condensation level the H_2O mixing ratio is vertically not constant. In particular, it is assumed constant below the condensation level and equal to the saturation mixing ratio above it. For this reason the optical depth and the transmittance are calculated in each step of the fitting loop because they depend on the vertical gas distribution. Finally the atmospheric transmittances of CO_2 and H_2O are multiplied with a high-resolution solar spectrum (Fiorenza and Formisano, 2005), which is corrected for the solar distance, the infrared reflectance (explained below) and the cosine of the incidence angle on the surface – whereas the reflection is assumed to be Lambertian. After that the convolution with the apodized instrumental function yields the absolute synthetic spectrum.

3.3 Normalization of the spectra

In order to prepare both the synthetic spectrum and the measured PFS spectrum for the retrieval they are divided by their specific continua to get a normalized synthetic spectrum $N_{syn}(\nu)$ and a normalized measured spectrum $N_{PFS}(\nu)$ in the range from $3700\,\mathrm{cm}^{-1}$ to $4100\,\mathrm{cm}^{-1}$. In case of the synthetic spectrum the continuum is assumed as linear and defined by two points that are not influenced by H_2O absorption. In Fig. 2 these points are marked as thick crosses (around $3774\,\mathrm{cm}^{-1}$ and $3908\,\mathrm{cm}^{-1}$) that define the linear con-

tinuum of the solar spectrum.

In order to get correct relative band depths for the synthetic spectrum its radiance level needs to be adjusted to the level of the measured spectrum. Hence the absolute synthetic spectrum I_{syn} is corrected for the incidence angle onto the surface and multiplied with a factor called reflectance. For this purpose the synthetic and the absolute PFS spectrum I_{PFS} are both averaged over a certain narrow wavenumber range. This range was selected from $3860\,\mathrm{cm}^{-1}$ to $3960\,\mathrm{cm}^{-1}$ because there the water band is not so strong and provides a reliable mean value due to its periodic form. Finally, the wavelength-independent reflectance A is determined when the equation $I_{PFS} = A \cdot I_{syn}$ is satisfied. However, the retrieved reflectance values are no real measurements because the PFS spectrum is not radiometrically calibrated.

The continuum of the averaged absolute PFS spectrum $I_{PFS}(\nu)$ is composed of a piecewise defined function $C(\nu)$ that is linear between two local maxima. A piecewise function was chosen in order to cope with possible wavenumber variations of the reflectance and the instrumental behavior. The mentioned local maximum is defined as a spectral point ν_M which has a higher radiance than its five adjacent spectral points[2]. Mathematically the normalized PFS spectrum is created by $N_{PFS}(\nu) = I_{PFS}(\nu) \,/\, C(\nu)$ where the wavenumber gridpoints ν are linearly interpolated between the local maxima ν_M. An example of such a piecewise continuum is shown in Fig. 3 as the dark grey line. The black crosses mark the local maxima before the continuum correction (explained below). The measured PFS spectrum is divided by this continuum

[2] The number of five provides generally the most reliable results compared to more or less stringent maxima.

resulting in the normalized PFS spectrum.

3.4 Fitting of the measured spectrum

In the performed least-square spectral fit the mixing ratio below the condensation level is the tuning parameter. The fitting criterion is defined as the standard deviation of the absolute difference of the normalized measured and synthetic spectra. This criterion is more robust for handling outlying data compared to the χ^2 criterion. It is applied in the range between $3820\,\mathrm{cm}^{-1}$ and $3900\,\mathrm{cm}^{-1}$ because there the water vapor lines are most pronounced and the influence of the solar spectrum is not too strong. The computation of the synthetic spectrum and its normalization are iterated in a loop using the steepest descent method to find the best fit (with Fibonacci minimization). The fitting loop stops when the optimum fit of the two spectra provides the H_2O mixing ratio with an accuracy of 1 ppm. The resulting number of the fitting criterion is taken as the value for the fit quality which is a measure for the perturbation of the spectrum due to instrumental behavior.

In the first iteration of the fitting loop the continuum used to normalize the measured spectrum is drawn directly through the local maxima. However, this ignores water absorption of up to a few percent in the continuum channels resulting in smaller band depth and an underestimation of the water abundance. Therefore the absorption is taken into account in a second fitting loop by slightly increasing the continuum of the synthetic spectrum of the first loop's best fit. So the radiance of the new maxima is given by $C_{new}(\nu_M) = I_{PFS}(\nu_M)\ /\ N^{opt}_{syn}(\nu_M)$ where $I_{PFS}(\nu_M)$ is the radiance of the absolute PFS spectrum and $N^{opt}_{syn}(\nu_M)$ the radiance of the normalized synthetic

spectrum with the optimum H_2O fit. Now the new corrected continuum is used to normalize the PFS spectrum again. The second iteration of the fitting loop yields the final result of water column density. In Fig. 3 this corrected continuum (dark grey line) is defined by the new local maxima (black diamonds) and used for normalization. Clearly in the region between 3790 cm^{-1} and 3890 cm^{-1} the continuum had to be shifted upwards for the purpose of getting an appropriate normalized spectrum which follows the expected band depth of a few percent.

3.5 Examples of spectral fits

Figure 4 displays a typical example of a spectral fit result for a good quality mean spectrum of orbit 278. The atmospheric profiles are calculated for latitude 6.7°N and longitude 15.5°W, during L_S=15.7° and local solar time (abbreviated with LST) of 11:03. However, despite the high signal of this measurement (S/N=166) and the good agreement of the spectra a few features remain not well fitted, e.g. the broader absorption around 3810 cm^{-1} or the more narrow line at 3852 cm^{-1}. The origin of these features, which are present in most of the spectra, is most likely an inaccurate line broadening factor in the model or even unknown contribution of atmospheric gases. Now Fig. 5 and Fig. 6 present two other examples with a lower radiance of the measurements. The first one is a spectrum representing an average signal-to-noise ratio of about 120 and the spectrum of Fig. 6 has a S/N of only 22. Still there is a satisfactory fit achieved.

3.6 Discussion of uncertainties

A vital issue of PFS/SW data analysis is the estimation of errors. A comparison of different databases for spectral lines, namely GEISA, HITRAN 2000 and HITRAN 2004 has shown minimal discrepancies. Regarding the calculation of transmittances the largest error source is certainly the factor for the spectral line broadening in CO_2 atmospheres. Although it is an important spectroscopic parameter there is little experimental information or even agreement on its exact value in the considered wavenumber range. To be able to quantify the retrieval error, the results of this work, using line parameters calculated according to Gamache et al. (1995), were compared with results that were produced with a constant line broadening parameter of 1.3 (e.g. used by Fedorova et al. (2006)). In this case the retrieved H_2O abundances differ by about 10–15%.

Also the effects of the used climate model were investigated. The pressure uncertainty of EMCD is estimated to be 10–20 Pa (F. Forget, private communication). As a consequence the column density results are less than 2% lower for a pressure shift of +10 Pa. To test the temperature dependence the EMCD temperature profile was shifted by ±3 K, and as a result the column density has changed by ±5%, mainly due to the shift of the saturation level. Note that the error in the formula for the determination of the saturation pressure (Eq. 1) is lower than the one due to the temperature uncertainty.

In the range between 3820 cm^{-1} and 3900 cm^{-1} the mean radiance of a single spectrum is approximately 0.6 erg $s^{-1}\,cm^{-2}\,sr^{-1}/cm^{-1}$ with a standard deviation of about 0.3 erg $s^{-1}\,cm^{-2}\,sr^{-1}/cm^{-1}$. Since there are generally 15 in-

dividual spectra averaged the S/N is improved by a factor of about 4. Hence the statistical error is for the majority of the measurements below 1.5%, the mean error is around 1%. Another error source originates from the fine-tuning of the wavenumber grid before the retrieval. The residual uncertainty on the result of the water amount is 1.5% in the worst case.

Regarding the systematic errors, the definition of the continuum both for the PFS spectra and for the synthetic spectra has the largest impact. The linear normalizing function for the synthetic spectrum is defined by two points around $3774\,\mathrm{cm}^{-1}$ and $3908\,\mathrm{cm}^{-1}$. Yet the final result for water vapor can vary by roughly 6% depending on the exact wavenumber of these points, e.g. by changing the second point from $3908\,\mathrm{cm}^{-1}$ to $3876\,\mathrm{cm}^{-1}$. The normalization of the measurements is another major source of uncertainties. Extensive testing of the piecewise defined continuum and its correction for H_2O absorption showed that results vary on average by 12%, even with only slight modifications of the continuum (cf. Tschimmel (2007)).

At last, there is also an intrinsic error of the fitting loop. If the true mixing ratio lies at the boundary of a fit interval the retrieved column density can differ by at most 6%. As a conclusion, the definition of the continuum is the major error source apart from the uncertainty due to the CO_2 line broadening factor. Considering all contributions the total error for each data point is therefore conservatively estimated to be 25%.

4 Results

4.1 Seasonal cycle

After processing the entire available dataset all those results were used for global analysis that fulfill the following criteria: the signal-to-noise ratio must be higher than 20 and the individual fit quality of a spectrum (defined in section 3.4) has to be better than the mean value plus five times the standard deviation of all fit qualities. Based on these results the seasonal map of atmospheric water for the period between the end of MY 26 at L_S=331° until the middle of MY 27 at L_S=196° is presented in Fig. 7 where the retrieved water column densities are binned by 2° in solar longitude (L_S) and 2° in geographic latitude. Such a bin contains on average 13 individual datapoints (maximum 88). Although the maximum binned column density is around 68 pr. µm the color scaling is only up to 60 pr. µm to emphasize the relative variations.

The average column density for the entire dataset is 16.2 pr. µm and in general the known evolution of the water cycle is followed. Before L_S=70° there is a mean H_2O content of 8.2 pr. µm detected. Although there is only a sparse coverage around L_S=70–75° it is clear that at this time the increase of atmospheric water content begins. The H_2O enhancement takes place at latitudes between 70°N and 80°N with mean values around 24 pr. µm. Between L_S=90° and about L_S=130° the latitudinal distribution is characterized by a gradient, spanning from column densities of 45–65 pr. µm north of 65°N, via 30–45 pr. µm between 55°N and 65°N and 20–30 pr. µm between 40°N and 55°N, down to values of 10–20 pr. µm between 0°N and 40°N and lower than 10 pr. µm south of the

equator. During L_S=130–140° the northern summer maximum drops rapidly to low amounts. At the same time a tongue-like peak of 15–20 pr. µm develops with a center around 45°N that migrates down to the equator arriving at about L_S=190°. The described behavior around northern summer was already seen in previous missions, namely by MAWD (Jakosky and Farmer, 1982), TES (Smith, 2004), SPICAM (Fedorova et al., 2006) and with the PFS/LW channel (Fouchet et al., 2007). Occurring differences between the reported values will be discussed in section 4.3.

To study the amount of water, that is transported from the north polar region towards the equator, in a quantitative way the column densities were binned within 5° of solar longitude and averaged in three latitudinal bands of 0–30°N, 30–60°N and 60–90°N. Then these mean column densities were multiplied with the respective surface area in order to estimate the total amount of atmospheric water contained in these latitudes. The resulting mass quantities are given in units of 10^{14} g of water and are displayed as a function of season in Fig. 8. During the maximum of the northern summer the mass of water mixed in the polar atmosphere is about $5 \cdot 10^{14}$ g in total (upper panel). In the latitudes between 30°N and 60°N (middle panel) it can even go up to $7 \cdot 10^{14}$ g. Although there the H_2O column densities are lower than further poleward they are overcompensated by the larger surface area. During L_S=130–145° the northern values drop rapidly to about $2 \cdot 10^{14}$ g while at the same time in the band of middle latitudes the total mass is still about $5 \cdot 10^{14}$ g. This is the period when the tongue-like feature starts moving southward. Now it is interesting to look at the lower panel. At 0–30°N the total mass experiences only a weak rise from about $4.5 \cdot 10^{14}$ g to approximately $5.5 \cdot 10^{14}$ g between L_S=110–130° and L_S=155–180°. During the same time the amounts in the

middle latitudes drop by about $2.5 \cdot 10^{14}$ g. All in all, the decrease of total mass in the polar region between summer and autumnal equinox (approx. $4 \cdot 10^{14}$ g) is not balanced by an equal increase in the middle latitudes and tropics later in the season. In these lower latitudes the atmospheric water content rises only by about $1 \cdot 10^{14}$ g. Thus it can be concluded that only about 25% of water vapor is transported southward via the atmospheric circulation while the majority of the water (approx. $3 \cdot 10^{14}$ g) has to be stored on the surface, either deposited as ice of the seasonal polar cap or adsorbed by the regolith in the higher latitudes (cf. Möhlmann (2004)). However, these values are only valid if the regolith in mid- and low-latitudes is inert, as assumed here. In case an interaction between the surface and the atmosphere takes place everywhere the amount is either under- or overestimated if the regolith acts as a sink or as a source, respectively.

4.2 Spatial variations

For the purpose of comparing spatial distributions it is useful to bin the averaged spectra in 2° longitude and 2° latitude within seasons that show little variability. In addition, to rule out topographic effects a scaling to 6.1 mbar is performed, i.e. the retrieved value of each datapoint is multiplied with $6.1/p_s$, where p_s [mbar] is the surface pressure. Hereby one has to keep in mind, though, that the scaling causes an overestimation of the water vapor in high-altitude regions like the Tharsis plateau in case the water is concentrated close to the surface and not equally mixed throughout the atmosphere. The scaled column density results, plotted over the albedo map of Mars, are displayed for L_S=330–75° in Fig. 9, for L_S=90–135° in Fig. 10 and for L_S=135–200° in

Fig. 11. In each figure the color scaling is adapted to the mean H_2O value. One feature is obvious in the figures around the equinoxes: over Arabia Terra there is an enhancement of a factor of about two compared to the mean column density. Over the Tharsis highlands another local maximum can be distinguished which is less pronounced, though. Even in the map of northern summer (Fig. 10) there are enhancements found in those two areas. Both maxima are visible in the PFS/LW maps of Fouchet et al. (2007) as well. Smith (2002) suggested an atmosphere–ground interaction as an explanation. Following the results of Möhlmann (2004) the increase over Arabia Terra is possibly explained by a regolith interaction via adsorption/desorption processes due to the strong correlation with hydrogen in the uppermost soil (reported by Feldman et al. (2004) and Mitrofanov et al. (2004)). However, these hydrogen maps of the *Odyssey* neutron spectrometers display another minor enhancement in the Medusae Fossae area, southwest of Olympus Mons, where no increased water vapor amount is observed. Even more, the Tharsis plateau with its H_2O maximum is basically devoid of hydrogen. These arguments in turn support the influence of atmospheric circulation and the presence of stationary waves which cause an accumulation of wet air over certain areas (Fedorova et al., 2004). The map with the entire dataset is displayed in Fig. 12 and strongly implies the existence of a stationary wave with two maxima and minima in the tropical latitudes. Yet Fouchet et al. (2007) performed simulations with the LMD/GCM that qualitatively reproduce the observed zonal water vapor asymmetry but do not reproduce the measured contrasts. Therefore a combination of both water exchange with the regolith and dynamical effects might be necessary to explain the observations (cf. Basilevsky et al. (2006)).

Now the northern summer maximum remains to be discussed in Fig. 10.

Clearly the highest column densities occur between 60°N and 85°N, centered around 75°N. Thus the bulk of the atmospheric water is located off the edges of the permanent polar cap which extends only to about 80°N. The seasonal cap is already fully retreated by L_S=90°. This observation was first interpreted by Haberle and Jakosky (1990) to be caused by atmospheric transport. Yet the relatively low column density of 29 pr. µm at L_S=70–75° leads to the conclusion that the subliming ice from the seasonal cap does not remain in the atmosphere. If this would be the case then one should see higher column densities. Montmessin et al. (2004) presented a convincing solution for this problem: the water vapor from the sublimation is transported by circulation further poleward and redeposited on the cold permanent ice cap. Later during the peak of the summer also this ice sublimes and produces the observed H_2O peak with approximately 60 pr. µm.

Another interesting point is the longitudinally inhomogeneous distribution of the water vapor near the polar cap. Between 30°W and 10°E there is a relative depletion which is not a seasonal effect as the orbits occurred at various L_S within the period L_S=90–135°. Another but weaker minimum is located at 110–120°W. On the other hand maxima can be identified as well, namely at 120–160°W which is identical with the maximum reported by Melchiorri et al. (2007), at 45–100°W and at 60–110°E. This unequal distribution might be a hint towards inhomogeneities in the process of sublimation and deposition in the polar area. These can be in turn caused by atmospheric wave phenomena, that accumulate moisture over certain preferred regions, or by properties of the underlying regolith, like its composition and adsorption capability.

4.3 Comparison with other observations

A comparison of the PFS/SW results with the ones of other instruments is given in this section. In particular, a look at the simultaneous observations from the two other spectrometers of *Mars Express*, OMEGA and SPICAM, is of interest. Principally the previous MAWD results (Fedorova et al., 2004) and the TES findings[3] are in agreement among each other and with the recent measurements of PFS/LW and OMEGA. Only SPICAM data[4] give systematically lower values which happens most likely due to stray light in the instrument optics (Fedorova et al., 2006). Now the results of this work are generally in agreement with all the spacecraft measurements during vernal equinox. For example, the column densities of 7–10 pr. µm, measured by TES (with the updated analysis) around ±20° latitude from the equator, agree well with the average value of 7.9 pr. µm that was found by PFS/SW. Also the approx. 8 pr. µm at 0–30°N reported by the PFS/LW team (Fouchet et al., 2007) are confirmed by PFS/SW (mean 8.3 pr. µm). Finally, the OMEGA spectra in the 2.6 µm band show column density values between 3 and 15 pr. µm, depending on the location (Melchiorri et al., 2007).

For possible interannual variations of the water cycle the northern summer can be interesting as it is the maximum throughout the year. The various results

[3] For this comparison not the originally published values of Smith (2004) were used but the results of a reanalysis of the TES dataset that was provided by M. Smith and is outlined by Fouchet et al. (2007) and Smith (2006).

[4] For the orbit comparisons not the originally published values of Fedorova et al. (2006) were used but the so far unpublished ones using the HITRAN 2004 line database (provided by A. Fedorova).

are as follows: maximum of about 75 pr. µm by MAWD, by TES (updated) maximum values of 55–65 pr. µm in MY 24, maxima of 60–70 pr. µm in MY 25 and 65–80 pr. µm in MY 26, only 55 pr. µm by SPICAM (with HITRAN 2000) during L_S=110–120°, for OMEGA at latitudes around 80°N Encrenaz et al. (2005) reported a mean maximum of 55 pr. µm during L_S=94–112° while Melchiorri et al. (2007) found a maximum with 40–70 pr. µm during L_S=93–126° and finally 30–60 pr. µm are the maximum values detected with PFS/LW. The retrieved column densities of this work are in good agreement with all those results as they range from 40 to 65 pr. µm north of 60°N. For the time around northern autumn equinox the various measurements are in similarly good agreement. Between the equator and northern low latitudes MAWD detected 15–20 pr. µm, TES (updated) on average 17 pr. µm, 10–12 pr. µm was seen at L_S=150° by SPICAM (with HITRAN 2000) and 10–18 pr. µm by the PFS/LW channel. PFS/SW delivers slightly higher values. For example during L_S=140–170° between 30°S and 30°N there are on average 12.4 pr. µm detected while PFS/LW finds values around 10 pr. µm. For L_S=165–200° the global mean values are approx. 12 pr. µm for the LW and 13.9 pr. µm for the SW channel. In conclusion, it is difficult to see significant differences in the amplitudes of atmospheric H_2O amounts between various martian years. This is due to the different samples in local time and geographic location and the large uncertainties for all retrievals (generally an error between 20% and 30% is stated). Therefore a constantly repeating water cycle seems to be present, at least for years without major dust storms.

At last, direct comparisons of three orbits are presented in Fig. 13 and Fig. 14. There the results of the different working groups are marked like this: red triangles are (updated) TES values by M. Smith, dark grey plus signs are

PFS/LW values by T. Fouchet, blue crosses are PFS/SW values of this work, green boxes are the EMCD 4.1 values, orange diamonds are OMEGA values by Maltagliati et al. (2007) and brown asterisk are SPICAM values (here with HITRAN 2004) by A. Fedorova. In the upper panels of the figures the saturation cutoff was determined by the temperature profile (cf. section 3.1) and in the lower panels all the water was confined below a height of 2.5 km above the surface (explained in the following section 4.4). In all figures the surface altitude is plotted below the results (solid black line), including the saturation level if it is lower than one scale height above the surface (dotted black line). For the *Mars Express* orbits up to number 770 there is an overlap in seasonal coverage with *MGS*/TES, so its (updated) results are presented, too. However, the TES spectra were recorded constantly at 14:00 local solar time and are not exactly from the same locations. The TES results are binned within $\pm 2.5^\circ$ of solar longitude and $\pm 3.75^\circ$ of topographic longitude. Considering these differences there is a good agreement between the results. Also the results of OMEGA, that are retrieved from the 2.6 µm band under consideration of saturation, are mainly in agreement with the results of this work. In contrast to that, the SPICAM amounts represent always the lowest boundary, apart from high latitudes in the northern summer. Fedorova et al. (2006) state stray light and instrumental effects as the reason for these deviations. Lastly, the theoretically expected column densities of the EMCD 4.1 database are presented as well and they are mostly higher than the measured ones. The reason for this is that up to now the EMCD water determination was calibrated with the original TES database and has to be corrected (F. Forget, private communication). In summary, the retrievals of all the instruments have errors in the order of 20–30%. Within these uncertainties the measurements are mainly consistent, apart from the values of SPICAM. The effect of the discrepancies

with the PFS/LW results will be addressed in the next section.

4.4 Vertical distribution

For the understanding of the vertical distribution of water vapor it is essential to know the altitude above the surface at which saturation occurs. With the used climate model and the retrieved water amounts its seasonal evolution is outlined as follows. Before vernal equinox the saturation level lies at 25 to 30 km and higher. As the northern summer approaches it drops to heights of about 15 km. During the northern summer the same values occur north of 70°, while more southward the saturation level is slightly lower, namely 10–15 km. Between L_S=130° and L_S=190° the saturation rises again at ±40° latitude from 10 km to 25 km and more. In general, the behavior matches the one shown by Smith (2002) very well.

Now regarding the actual vertical distribution below the saturation level there is still a controversy if water vapor is equally mixed with CO_2 or distributed in a more complex way. The comparison of the PFS/SW results with the ones of PFS/LW by Fouchet et al. (2007) allows an assessment of the vertical distribution of water vapor (Formisano et al., 2004) due to the different sensitivity of the SW and LW spectral features to the vertical H_2O profile. In the following the PFS/LW results are used as the reference because they do not differ much between a retrieval with equal mixing and one with a confinement to the first model layer. It can be seen in the upper panels of Fig. 13 and Fig. 14 that the SW values are often higher than the LW results. This difference is the strongest in Fig. 14 (northern summer) over northern high-latitude areas. For a broader investigation the SW results were divided by the equally binned LW

ones. The resulting ratio of the water abundance retrieved from SW spectra to that derived from LW spectra is displayed versus L_S in Fig.15. Clearly, in summer the SW abundances have a pronounced maximum northward of 50°N where they are by a factor of 2 and more higher than the LW ones. The second maximum in the tropics is reduced in absolute values due to the lower H_2O amounts there.

One way to explain this finding might be the instrumental behavior and different retrievals because the absolute difference between the SW and the LW results is larger with a higher atmospheric water content. Of course, various tests of the retrieval method, as indicated in section 3.6, were conducted in order to reduce the difference between the two PFS channels. However, since this difference persisted to significantly exceed uncertainties in water retrievals from both PFS channels in the season of high activity of the surface sources, an explanation related to strong non-uniformity of the H_2O vertical distribution seemed more plausible. Therefore test retrievals were carried out with the assumption that all water is confined to the lower 2.5 km – the planetary boundary layer. This results in a lower retrieved column density (while the mixing ratio at the surface is higher) since less water is necessary in total to fit the observed spectral depth because the absorption lines are subject to greater pressure broadening.

The results of the test retrievals using confinement are displayed in the lower panels of Fig. 13 and Fig. 14. Interestingly, the agreement with the PFS/LW results is now much better in many cases, especially for the northern summer observations. One might argue that the LW retrievals have a varying saturation level depending on the atmospheric temperature while the SW retrievals have all a fixed cutoff. However, Fouchet et al. (2007) have shown, in particular

for orbit 1023 southward of about 72°N, that for the LW channel the resulting H_2O amounts depend only very weakly on the applied vertical distribution. Only in the highest polar latitudes PFS/LW is sensitive to the water profile due to the lower thermal contrast between the surface and the atmosphere. So it is reasonable to assume that for locations with large differences in column densities the atmospheric water is not equally mixed with CO_2 but follows another vertical distribution which keeps the H_2O more confined to the surface. Please note that the confinement to 2.5 km was arbitrarily chosen and is not considered as a measurement of the vertical distribution. Changing confinement height values and more complex water distributions are expected to deliver more accurate and consistent agreements. In fact, the used confinement could lead to the conclusion that the larger the relative difference is in Fig.15 the lower the confinement has to be. However, this makes the observed spatial and seasonal pattern very hard to explain.

A physical explanation for the water confinement to a shallow layer above the surface could be a fast supply of water vapor from the ground, e.g. driven by solar forcing, and an efficient mixing within the boundary layer due to convection and turbulent eddies. The time scale of eddy mixing is given by $\tau = H(z)^2/\epsilon(z)$ with the scale height $H(z)$ and the eddy mixing coefficient $\epsilon(z)$ which are both a function of height (Titov et al., 1994). Within the boundary layer the coefficient is $\epsilon \approx 10^7 - 10^8\,\mathrm{cm^2\,s^{-1}}$ while in the atmosphere above it is $\epsilon \approx 10^6\,\mathrm{cm^2\,s^{-1}}$. This yields timescales of roughly one day in the lowest few kilometers and of many days or weeks in the free atmosphere. Hence active ground sources like ice sublimation or H_2O desorption from regolith can keep the boundary layer filled with water vapor. As transport further upward is a much slower process the bulk of the atmospheric H_2O is confined to few

kilometers above the surface.

So the conclusion is that water vapor does often not obey an equal mixing with CO_2 but is more confined to the surface within the boundary layer. In accordance with Fouchet et al. (2007) an intermediate way between confinement and uniform mixing seems reasonable, and the importance of a gas exchange between the atmosphere and the surface is emphasized. This result implies also that the OMEGA results need to be corrected because they are gained from the 2.6 µm band, too. Finally, a combined retrieval of PFS/LW and PFS/SW, including the temperature retrieval from the LW channel and various vertical H_2O distributions, could promise an even better understanding of the vertical behavior of water vapor on Mars.

5 Conclusions

In this work the available dataset of the SW channel of PFS up to orbit 1609 was analyzed in the 2.6 µm band to sound the atmosphere of Mars for water vapor. The applied technique of relative band depth fitting was explicitly described in section 3, including the explanation of the total error of 25% for each averaged spectrum. The results for the time between L_S=331° of MY 26 and L_S=196° of MY 27 are summarized in the following. Please note that after L_S=83° only *Mars Express* was monitoring the atmosphere for water vapor in MY 27. Thus the PFS dataset is crucial for a continuous coverage of the H_2O cycle.

(1) One of the main goals of PFS is to characterize the martian water cycle with great temporal resolution. In the covered period of a little more than

the first half year of MY 27 an average column density of 16.2 pr. µm is found. This high amount is due to fact that the subliming polar cap of the northern summer dominates this time. In the relatively dry equinox season before L_S=70° there is a mean water content of 8.2 pr. µm in the atmosphere. After that the northern seasonal polar cap retreats and the subliming ice enriches the atmosphere with water. The center of this H_2O increase is around 75°N, and during L_S=90–130° abundances of more than 50 pr. µm are measured in this region (maximum binned value 68 pr. µm). Towards the equator there is a steep gradient of 50 pr. µm at about 70°N latitude, 20–40 pr. µm between 40°N and 60°N and down to values of 10–20 pr. µm and lower southward of 40°N. Finally, after L_S=135° the summer maximum quickly vanishes and a tongue-like peak of 15–20 pr. µm develops that moves towards the equator which is reached at L_S=190°. The driving force behind this movement is the atmospheric circulation. However, the net amount of transported water mass that arrives in the northern equatorial region (approximately $1 \cdot 10^{14}$ g) is much smaller than the amount released during the previous summer (about $4 \cdot 10^{14}$ g). Thus the bulk of the atmospheric water must be deposited as ice on the ground or adsorbed by the soil.

(2) The quantitative comparison of the water vapor retrievals from the thermal part of the IR spectrum (PFS/LW) with those of the near-infrared part (PFS/SW) yielded the next important conclusion because it permits an assessment of the vertical distribution of H_2O. For the northern summer season the LW values northward of approximately 50°N are significantly lower than those of this work. While the LW channel is only marginally dependent on the vertical distribution the SW retrievals exhibit strong differences with changing vertical concentrations. Far bet-

ter agreements between both findings are achieved by deviating from an equally mixed H_2O distribution up to the saturation level to a confinement of the water within the lower 2–3 km above the surface. A physical explanation for this phenomenon could be a rapid increase of H_2O coming from the soil. This water vapor then undergoes quick vertical mixing by turbulent eddies within the boundary layer at timescales in the order of a day. However, at higher altitudes in the free atmosphere only slow mixing by diffusion takes place with timescales of many days. Therefore the water vapor stays confined to the lower few kilometers of the atmosphere.

(3) The spatial distribution of water is characterized by two local maxima over Arabia Terra and the Tharsis highlands. There the column densities, scaled to 6.1 mbar, are by a factor of about two higher compared to the adjacent regions of the same latitudes. This detection confirms earlier measurements and is best explained by a combination of both regolith–atmosphere interaction and atmospheric forcing by stationary planetary waves because neither of them can explain these wave-like features alone.

(4) Another interesting phenomenon is the uneven longitudinal distribution of the north pole maximum between 65°N and 85°N that might be caused by inhomogeneous sublimation and deposition processes. A broad depletion of atmospheric water is found between 30°W and 10°E and a smaller one at 110–115°W whereas high concentrations of H_2O are detected at 120–160°W, at 45–100°W and at 60–110°E. Physical reasons for these phenomena could be atmospheric circulation or specific properties of the soil that interacts with the atmosphere.

(5) In general, the observed abundances are mostly in agreement with previous results of groundbased observations, of the orbiting *Viking*/MAWD and *MGS*/TES spectrometers, and results of simultaneous observations

by SPICAM, OMEGA and PFS/LW onboard *Mars Express* (within the respective errors of typically 20–30%). Occurring discrepancies, like the SPICAM results being systematically lower or the PFS/SW results being on average slightly higher than the PFS/LW ones, can be attributed to the various applied retrieval techniques and instrumental behavior.

Regarding more recent data processing, PFS resumed operations in November 2005 after a gap of several weeks and is operating smoothly since then. The new results will be presented in the future.

Acknowledgements

We would like to express our gratitude to Mike Smith who kindly provided the updated TES database and strongly supported us with valuable discussions. In addition, we would like to thank Anna Fedorova and Luca Maltagliati for providing us with the latest retrievals from SPICAM and OMEGA, respectively. Their contribution helped to compare and understand the results from different instruments which was done as part of a workshop at the ISSI in Bern, Switzerland. We thank ISSI for the valuable support.

References

Basilevsky, A. T., Rodin, A. V., Raitala, J., Neukum, G., Werner, S., Kozyrev, A. S., Sanin, A. B., Mitrofanov, I. G., Head, J. W., Boynton, W., Saunders, R. S., Oct. 2006. Search for causes of the low epithermal neutron flux anomaly in the Arabia Terra region (Mars). Solar System Research 40, 355–374.

Clancy, R. T., Sandor, B. J., Wolff, M. J., Christensen, P. R., Smith, M. D., Pearl, J. C., Conrath, B. J., Wilson, R. J., Apr. 2000. An intercomparison of ground-based millimeter, MGS TES, and Viking atmospheric temperature measurements: Seasonal and interannual variability of temperatures and dust loading in the global Mars atmosphere. J. Geophys. Res.105, 9553–9572.

Comolli, L., Saggin, B., 2005. Evaluation of the sensitivity to mechanical vibrations of an IR Fourier spectrometer. Review of Scientific Instruments 76 (12), 123112.

Encrenaz, T., Melchiorri, R., Fouchet, T., Drossart, P., Lellouch, E., Gondet, B., Bibring, J.-P., Langevin, Y., Titov, D., Ignatiev, N., Forget, F., Oct. 2005. A mapping of martian water sublimation during early northern summer using OMEGA/Mars Express. Astron. Astrophys.441, L9–L12.

Fedorova, A., Korablev, O., Bertaux, J.-L., Rodin, A., Kiselev, A., Perrier, S., Sep. 2006. Mars water vapor abundance from SPICAM IR spectrometer: Seasonal and geographic distributions. J. Geophys. Res.111, 9.

Fedorova, A. A., Rodin, A. V., Baklanova, I. V., Sep. 2004. MAWD observations revisited: seasonal behavior of water vapor in the martian atmosphere. Icarus 171, 54–67.

Feldman, W. C., Prettyman, T. H., Maurice, S., Plaut, J. J., Bish, D. L., Van-

iman, D. T., Mellon, M. T., Metzger, A. E., Squyres, S. W., Karunatillake, S., Boynton, W. V., Elphic, R. C., Funsten, H. O., Lawrence, D. J., Tokar, R. L., Sep. 2004. Global distribution of near-surface hydrogen on Mars. J. Geophys. Res.109, 9006.

Fiorenza, C., Formisano, V., Aug. 2005. A solar spectrum for PFS data analysis. Planet. Space Sci.53, 1009–1016.

Forget, F., Hourdin, F., Fournier, R., Hourdin, C., Talagrand, O., Collins, M., Lewis, S. R., Read, P. L., Huot, J.-P., Oct. 1999. Improved general circulation models of the Martian atmosphere from the surface to above 80 km. J. Geophys. Res.104, 24155–24176.

Forget, F., Millour, E., Lebonnois, S., Montabone, L., Dassas, K., Lewis, S. R., Read, P. L., López-Valverde, M. A., González-Galindo, F., Montmessin, F., Lefèvre, F., Desjean, M.-C., Huot, J.-P., Feb. 2006. The new Mars climate database. In: Forget, F., Lopez-Valverde, M. A., Desjean, M. C., Huot, J. P., Lefevre, F., Lebonnois, S., Lewis, S. R., Millour, E., Read, P. L., Wilson, R. J. (Eds.), Mars Atmosphere Modelling and Observations. p. 128.

Formisano, V., Angrilli, F., Arnold, G., Atreya, S., Bianchini, G., Biondi, D., Blanco, A., Blecka, M. I., Coradini, A., Colangeli, L., Ekonomov, A., Esposito, F., Fonti, S., Giuranna, M., Grassi, D., Gnedykh, V., Grigoriev, A., Hansen, G., Hirsh, H., Khatuntsev, I., Kiselev, A., Ignatiev, N., Jurewicz, A., Lellouch, E., Lopez Moreno, J., Marten, A., Mattana, A., Maturilli, A., Mencarelli, E., Michalska, M., Moroz, V., Moshkin, B., Nespoli, F., Nikolsky, Y., Orfei, R., Orleanski, P., Orofino, V., Palomba, E., Patsaev, D., Piccioni, G., Rataj, M., Rodrigo, R., Rodriguez, J., Rossi, M., Saggin, B., Titov, D., Zasova, L., Aug. 2005. The Planetary Fourier Spectrometer (PFS) onboard the European Mars Express mission. Planet. Space Sci.53, 963–974.

Formisano, V., Grassi, D., Orfei, R., Biondi, D., Mencarelli, E., Mattana, A.,

Nespoli, F., Maturilli, A., Giuranna, M., Rossi, M., Maggi, M., Baldetti, P., Chionchio, G., Saggin, B., Angrilli, F., Bianchini, G., Piccioni, G., di Lellis, A., Cerroni, P., Capaccioni, F., Capria, M. T., Coradini, A., Fonti, S., Orofino, V., Blanco, A., Colangeli, L., Palomba, E., Esposito, F., Patsaev, D., Moroz, V., Zasova, L., Ignatiev, N., Khatuntsev, I., Moshkin, B., Ekonomov, A., Grigoriev, A., Nechaev, V., Kiselev, A., Nikolsky, Y., Gnedykh, V., Titov, D., Orleanski, P., Rataj, M., Malgoska, M., Jurewicz, A., Blecka, M. I., Hirsh, H., Arnold, G., Lellouch, E., Marten, A., Encrenaz, T., Lopez Moreno, J., Atreya, Gobbi, P. S., Aug. 2004. PFS: the Planetary Fourier Spectrometer for Mars Express. In: Wilson, A., Chicarro, A. (Eds.), ESA Special Publication. Vol. 1240 of ESA Special Publication. pp. 71–94.

Fouchet, T., Lellouch, E., Ignatiev, N. I., Forget, F., Titov, D. V., Tschimmel, M., Montmessin, F., Formisano, V., Giuranna, M., Maturilli, A., Encrenaz, T., Sep. 2007. Martian water vapor: Mars Express PFS/LW observations. Icarus 190, 32–49.

Gamache, R. R., Neshyba, S. P., Plateaux, J. J., Barbe, A., Régalia, L., Pollack, J. B., Mar. 1995. CO_2-broadening of water-vapor lines. J. Mol. Spectrosc. 170, 131–151.

Giuranna, M., Formisano, V., Biondi, D., Ekonomov, A., Fonti, S., Grassi, D., Hirsch, H., Khatuntsev, I., Ignatiev, N., Michalska, M., Mattana, A., Maturilli, A., Moshkin, B. E., Mencarelli, E., Nespoli, F., Orfei, R., Orleanski, P., Piccioni, G., Rataj, M., Saggin, B., Zasova, L., Aug. 2005. Calibration of the Planetary Fourier Spectrometer short wavelength channel. Planet. Space Sci.53, 975–991.

Giuranna, M., Hansen, G., Maturilli, A., Zasova, L., Formisano, V., Grassi, D., Ignatiev, N., 2007. Spatial variability, composition and thickness of the seasonal north polar cap of Mars in mid-spring. Planet. Space Sci., in press

.

Haberle, R. M., Jakosky, B. M., Feb. 1990. Sublimation and transport of water from the north residual polar CAP on Mars. J. Geophys. Res.95, 1423–1437.

Haus, R., Titov, D. V., Oct. 2000. PFS on Mars Express: preparing the analysis of infrared spectra to be measured by the Planetary Fourier Spectrometer. Planet. Space Sci.48, 1357–1376.

Jakosky, B. M., Farmer, C. B., Apr. 1982. The seasonal and global behavior of water vapor in the Mars atmosphere - Complete global results of the Viking atmospheric water detector experiment. J. Geophys. Res.87, 2999–3019.

Krasnopol'skii, V. A., Korablev, O. I., Moroz, V. I., Krysko, A. A., Blamont, J. E., Chassefiere, E., Nov. 1991. Infrared solar occultation sounding of the Martian atmosphere by the Phobos spacecraft. Icarus 94, 32–44.

Lewis, S. R., Collins, M., Read, P. L., Forget, F., Hourdin, F., Fournier, R., Hourdin, C., Talagrand, O., Huot, J.-P., Oct. 1999. A climate database for Mars. J. Geophys. Res.104, 24177–24194.

Maltagliati, L., Titov, D. V., Encrenaz, T., Melchiorri, R., Forget, F., Garcia-Comas, M., Keller, H. U., Langevin, Y., Bibring, J.-P., 2007. Observations of atmospheric water vapor above the Tharsis volcanoes on Mars with the OMEGA/MEx imaging spectrometer. Icarus, in press .

Mauersberger, K., Krankowsky, D., Feb. 2003. Vapor pressure above ice at temperatures below 170 K. Geophys. Res. Lett.30, 21–1.

Melchiorri, R., Encrenaz, T., Fouchet, T., Drossart, P., Lellouch, E., Gondet, B., Bibring, J.-P., Langevin, Y., Schmitt, B., Titov, D., Ignatiev, N., Feb. 2007. Water vapor mapping on Mars using OMEGA/Mars Express. Planet. Space Sci.55, 333–342.

Mitrofanov, I. G., Litvak, M. L., Kozyrev, A. S., Sanin, A. B., Tret'yakov, V. I., Grin'kov, V. Y., Boynton, W. V., Shinohara, C., Hamara, D., Saunders,

R. S., Jul. 2004. Soil Water Content on Mars as Estimated from Neutron Measurements by the HEND Instrument Onboard the 2001 Mars Odyssey Spacecraft. Solar System Research 38, 253–257.

Möhlmann, D. T. F., Apr. 2004. Water in the upper martian surface at mid- and low-latitudes: presence, state, and consequences. Icarus 168, 318–323.

Montmessin, F., Forget, F., Rannou, P., Cabane, M., Haberle, R. M., Oct. 2004. Origin and role of water ice clouds in the Martian water cycle as inferred from a general circulation model. J. Geophys. Res.109, 10004.

Rosenqvist, J., Drossart, P., Combes, M., Encrenaz, T., Lellouch, E., Bibring, J. P., Erard, S., Langevin, Y., Chassefière, E., Aug. 1992. Minor constituents in the Martian atmosphere from the ISM/Phobos experiment. Icarus 98, 254–270.

Rothman, L. S., Jacquemart, D., Barbe, A., Benner, D. C., Birk, M., Brown, L. R., Carleer, M. R., Chackerian, C., Chance, K., Coudert, L. H., Dana, V., Devi, V. M., Flaud, J. M., Gamache, R. R., Goldman, A., Hartmann, J. M., Jucks, K. W., Maki, A. G., Mandin, J. Y., Massie, S. T., Orphal, J., Perrin, A., Rinsland, C. P., Smith, M. A. H., Tennyson, J., Tolchenov, R. N., Toth, R. A., Vander Auwera, J., Varanasi, P., Wagner, G., Dec. 2005. The HITRAN 2004 molecular spectroscopic database. J. Quant. Spectrosc. Rad. Transfer 96, 139–204.

Smith, M. D., Nov. 2002. The annual cycle of water vapor on Mars as observed by the Thermal Emission Spectrometer. J. Geophys. Res.107, 25–1.

Smith, M. D., Jan. 2004. Interannual variability in TES atmospheric observations of Mars during 1999-2003. Icarus 167, 148–165.

Smith, M. D., Feb. 2006. TES atmospheric temperature, aerosol optical depth, and water vapor observations 1999-2004. In: Forget, F., Lopez-Valverde, M. A., Desjean, M. C., Huot, J. P., Lefevre, F., Lebonnois, S., Lewis, S. R.,

Millour, E., Read, P. L., Wilson, R. J. (Eds.), Mars Atmosphere Modelling and Observations. p. 211.

Spinrad, H., Münch, G., Kaplan, L. D., May 1963. Letter to the Editor: the Detection of Water Vapor on Mars. Astrophys. J.137, 1319.

Sprague, A. L., Hunten, D. M., Doose, L. R., Hill, R. E., May 2003. Mars atmospheric water vapor abundance: 1996-1997. Icarus 163, 88–101.

Sprague, A. L., Hunten, D. M., Doose, L. R., Hill, R. E., Boynton, W. V., Smith, M. D., Pearl, J. C., Oct. 2006. Mars atmospheric water vapor abundance: 1991–1999, emphasis 1998–1999. Icarus 184, 372–400.

Sprague, A. L., Hunten, D. M., Hill, R. E., Doose, L. R., Rizk, B., Nov. 2001. Water Vapor Abundances over Mars North High Latitude Regions: 1996-1999. Icarus 154, 183–189.

Sprague, A. L., Hunten, D. M., Hill, R. E., Rizk, B., Wells, W. K., 1996. Martian water vapor, 1988-1995. J. Geophys. Res.101, 23229–23254.

Titov, D. V., Haus, R., Mar. 1997. A fast and accurate method of calculation of gaseous transmission functions in planetary atmospheres. Planet. Space Sci.45, 369–377.

Titov, D. V., Markiewicz, W. J., Thomas, N., Keller, H. U., Sablotny, R. M., Tomasko, M. G., Lemmon, M. T., Smith, P. H., Apr. 1999. Measurements of the atmospheric water vapor on Mars by the Imager for Mars Pathfinder. J. Geophys. Res.104, 9019–9026.

Titov, D. V., Moroz, V. I., Grigoriev, A. V., Rosenqvist, J., Combes, M., Bibring, J.-P., Arnold, G., Nov. 1994. Observations of water vapour anomaly above Tharsis volcanoes on Mars in the ISM (Phobos-2) experiment. Planet. Space Sci.42, 1001–1010.

Tschimmel, M., 2007. Investigation of the atmospheric water cycle on Mars by the Planetary Fourier Spectrometer onboard Mars Express. Ph.D. thesis,

Copernicus GmbH, ISBN 978-3-936586-63-3.

Figure captions

Fig. 1: The coverage of local solar time and season for all processed datapoints.

Fig. 2: Normalization of the synthetic spectrum (black curve): definition of the linear continuum of the solar spectrum (grey curve) by two points that are not affected by water absorption (thick crosses at 3774 cm^{-1} and 3908 cm^{-1}). The presented synthetic spectrum corresponds to a mixing ratio of 300 ppm.

Fig. 3: The normalized PFS spectrum (upper black curve) is created from the average of the absolute PFS spectra 134–148 of orbit 1549 (light grey curve) by its division through the piecewise defined continuum (dark grey line). In the first iteration of the fitting loop the continuum definition points are selected (black crosses) and in the second iteration they are corrected for H_2O continuum absorption (black diamonds).

Fig. 4: The normalized PFS spectrum (black line), that is created from the observational spectra 61–75 of orbit 278, is fitted by the synthetic spectrum (grey line). For the H_2O fitting the region between 3820 cm^{-1} and 3900 cm^{-1} was used yielding a mixing ratio of 225 ppm corresponding to a column density of 19.0 pr. µm at a saturation level of 19 km above the surface.

Fig. 5: The average spectrum 258–272 of orbit 1549 with a S/N ratio of about 120 shows water with 156 ppm or 8 pr. µm (saturation level at 35 km).

Fig. 6: The average spectrum 115–129 of orbit 1055 with a low S/N=22 is fitted with water with 482 ppm or 31.8 pr. µm (saturation level at 9 km).

Fig. 7: The seasonal map of water vapor between L_S=330° of MY 26 and L_S=200° of MY 27. The martian H_2O cycle is well covered in this period and shows a clear summer maximum (the highest value is 68 pr. µm).

Fig. 8: For the three latitude bands of 60–90°N (upper panel), 30–60°N (middle panel) and 0–30°N (lower panel) the retrieved column densities were binned within 5° of L_S and multiplied with the respective area to get the total amount of water contained in the atmosphere of that latitude (given in 10^{14} g). Further explanations are given in the text.

Fig. 9: The spatial distribution of water vapor for L_S=330–75° (northern spring). The column densities, normalized to 6.1 mbar, are displayed up to 20 pr. µm.

Fig. 10: The spatial distribution of water vapor for L_S=90–135° (northern summer). The column densities, normalized to 6.1 mbar, are displayed up to 50 pr. µm.

Fig. 11: The spatial distribution of water vapor for L_S=135–200° (northern autumn). The column densities, normalized to 6.1 mbar, are displayed up to 30 pr. µm.

Fig. 12: The spatial distribution of water vapor for the entire processed dataset. The column densities, normalized to 6.1 mbar, are displayed up to 40 pr. µm.

Fig. 13: Results of various instruments for orbit 348 (L_S=26°) with regular saturation cutoff (upper panel) and with a confinement below 2.5 km for the

PFS/SW retrievals (lower panel).

Fig. 14: Results of various instruments for orbit 1023 (L_S=111°) with regular saturation cutoff (upper panel) and with a confinement below 2.5 km for the PFS/SW retrievals (lower panel).

Fig. 15: The seasonal evolution of the column density ratio between the PFS/SW and the PFS/LW channel. The higher absolute H_2O amount in the polar region during northern summer naturally means a higher difference in absolute values between both results.

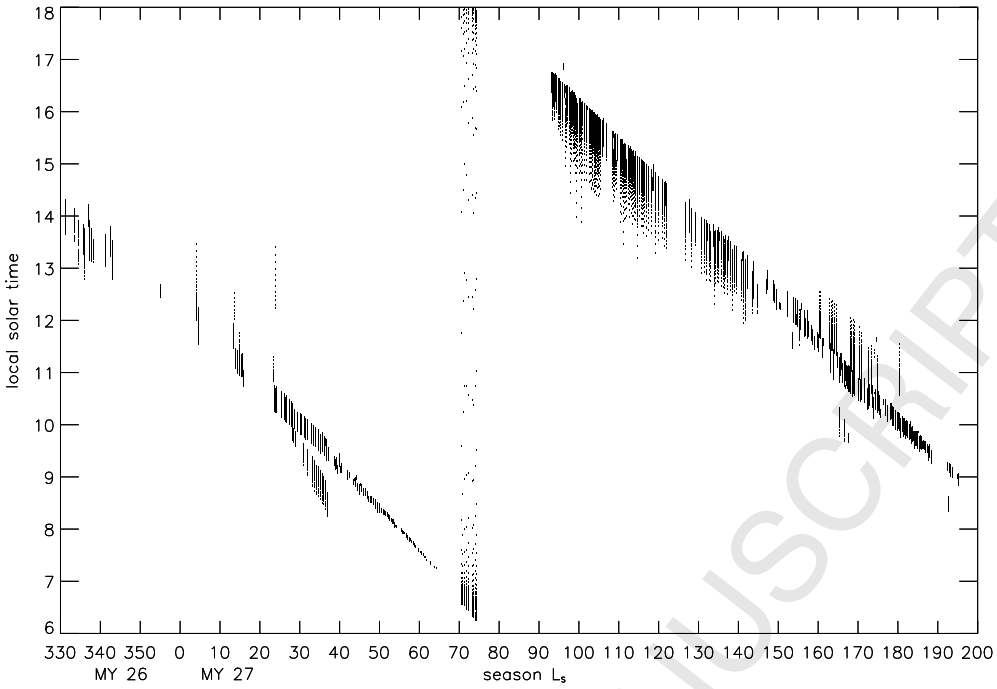

Fig. 1.

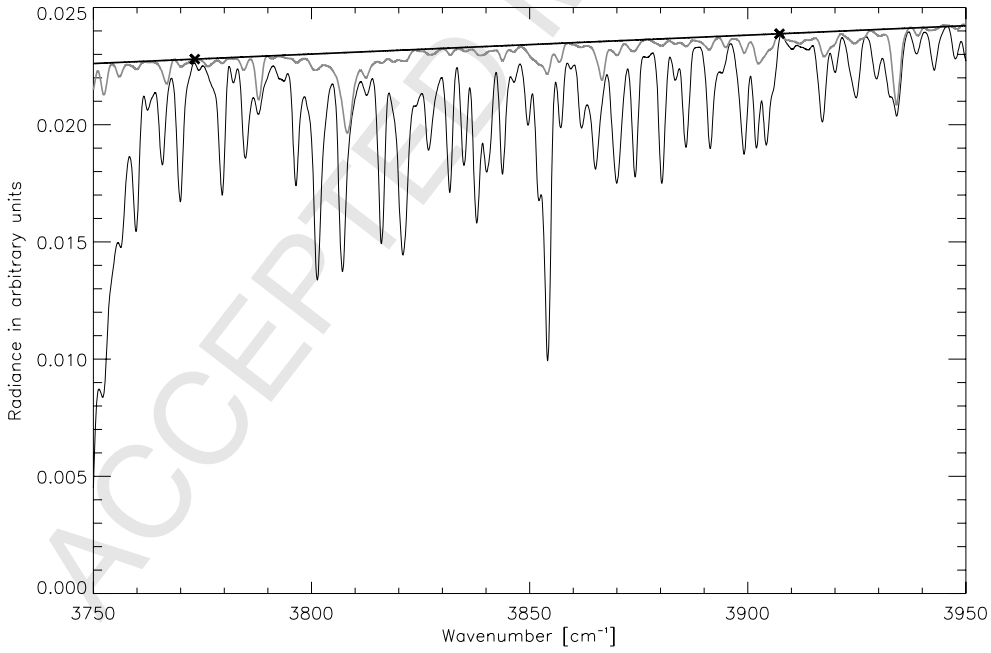

Fig. 2.

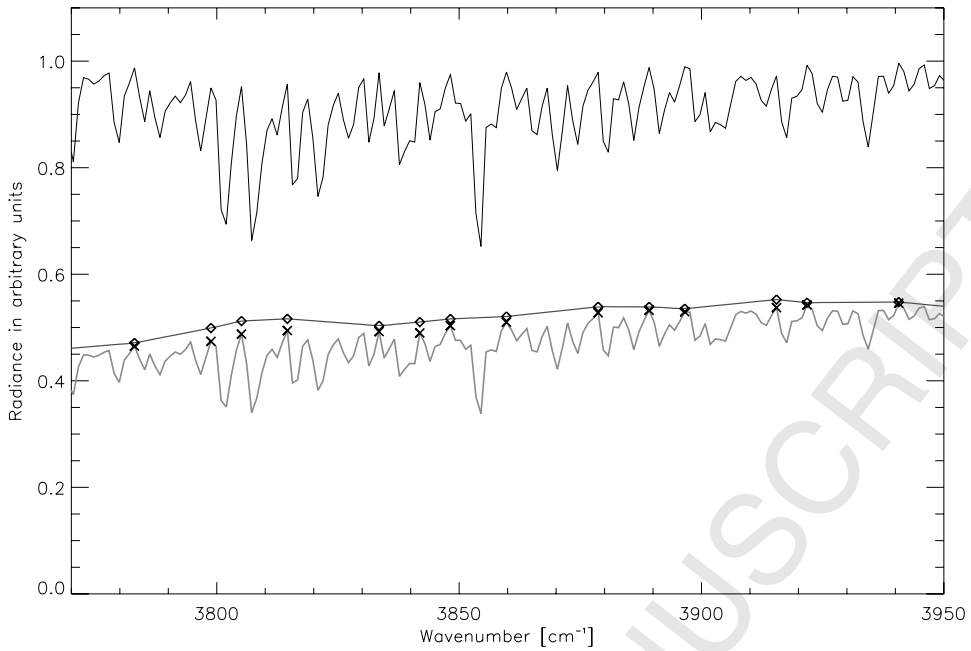

Fig. 3.

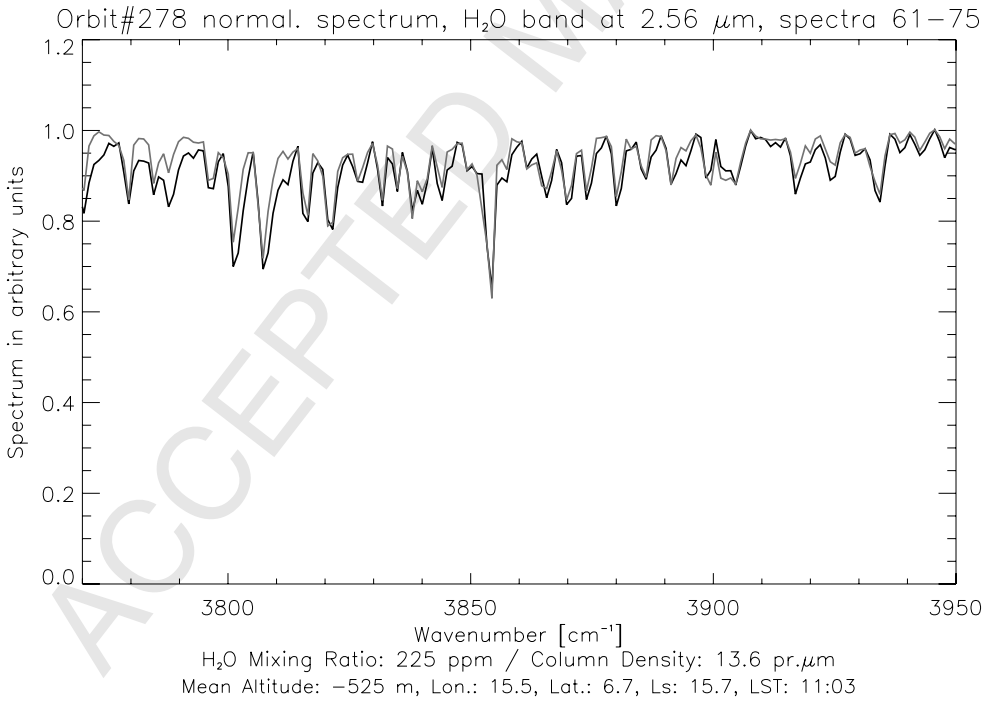

Fig. 4.

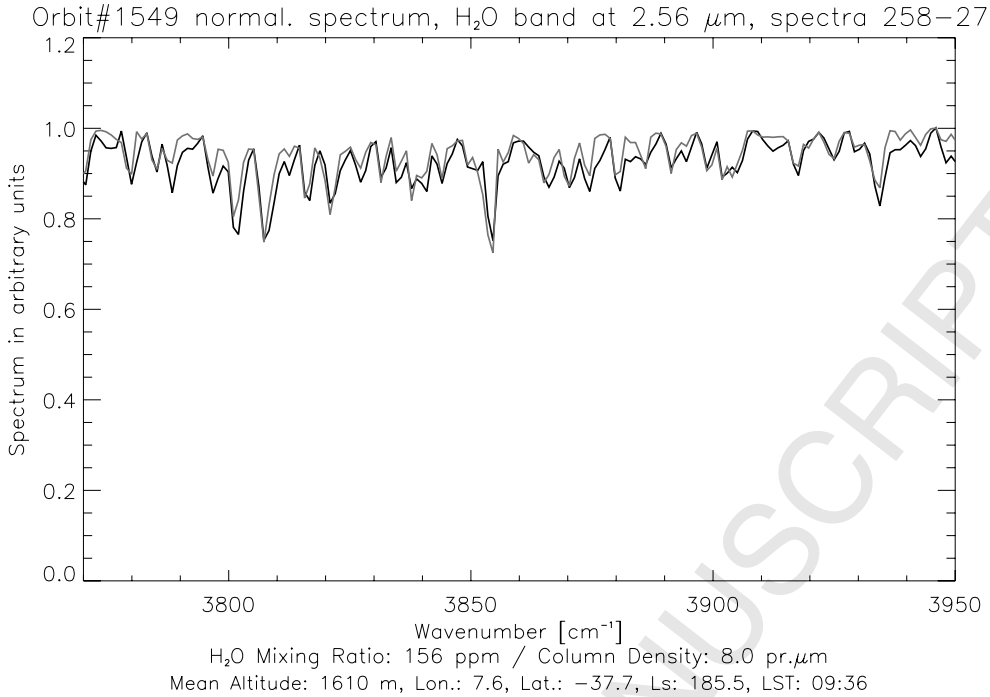

Fig. 5.

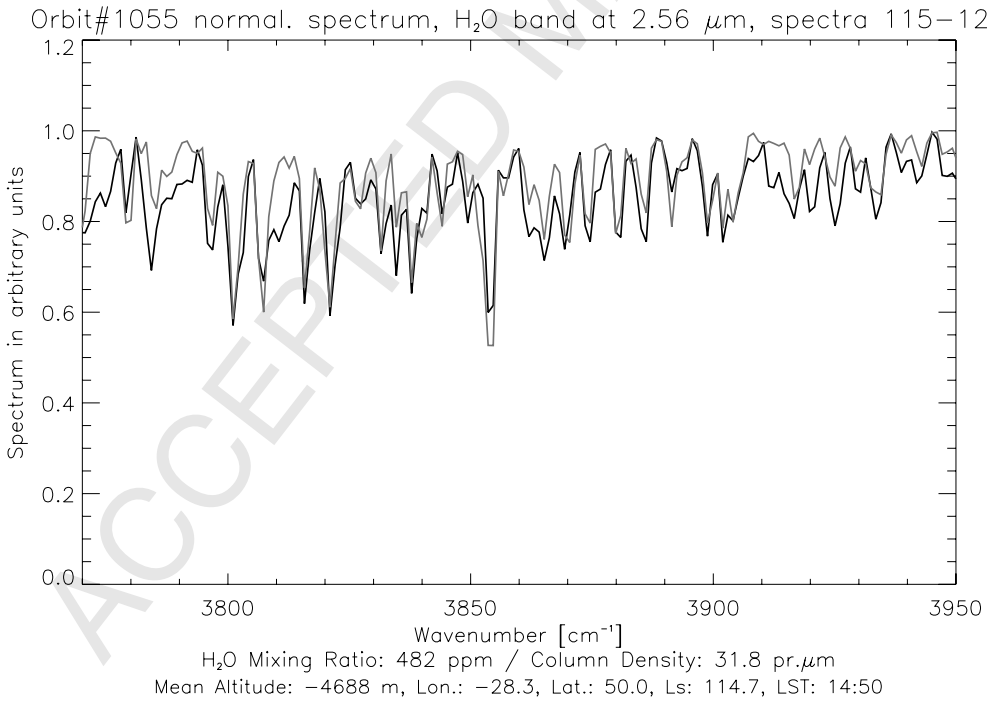

Fig. 6.

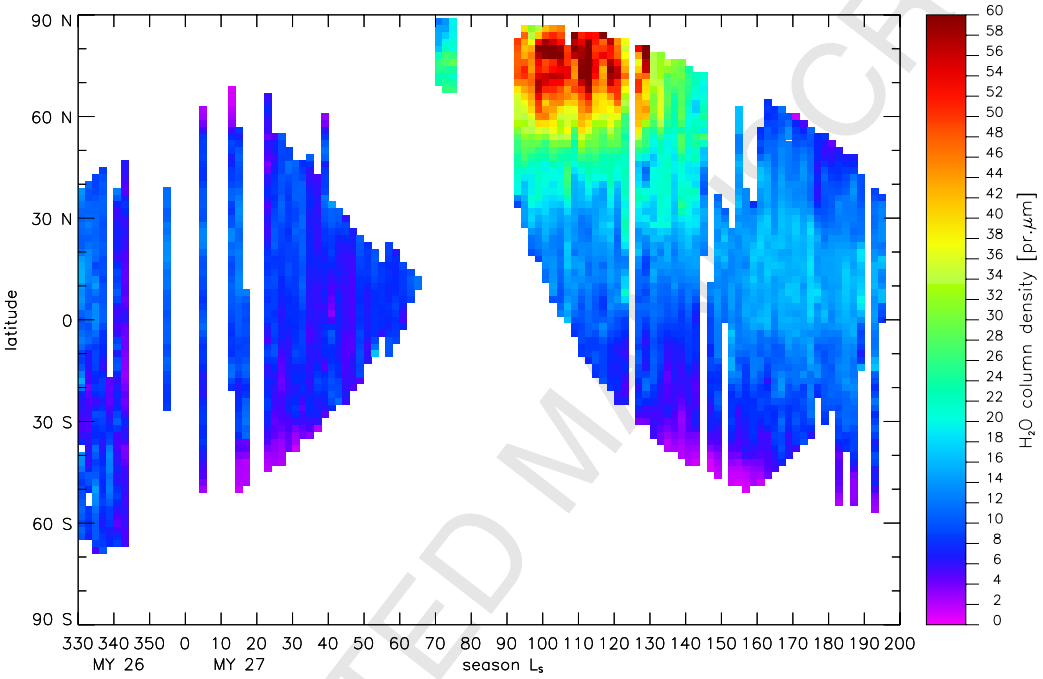

Fig. 7.

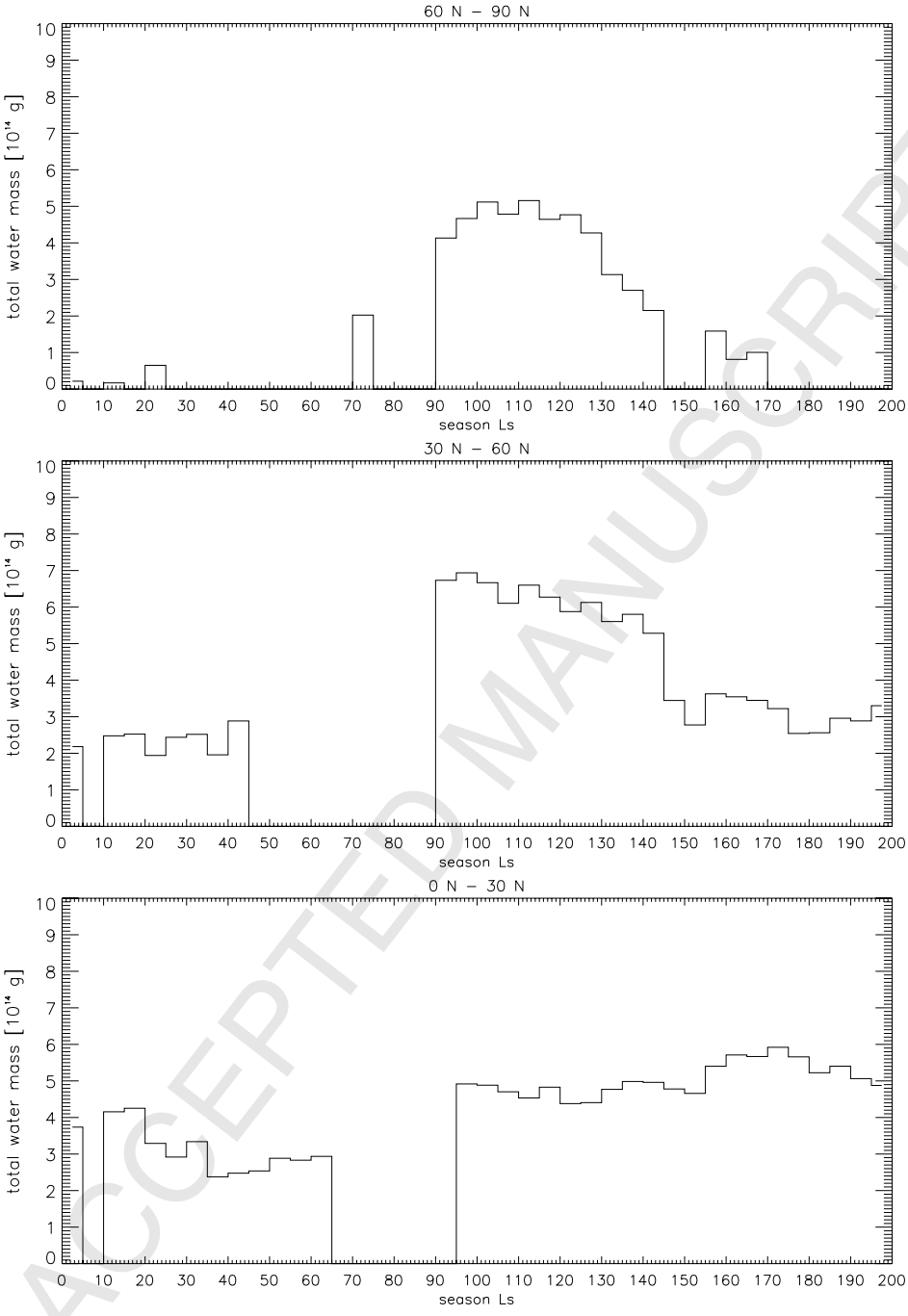

Fig. 8.

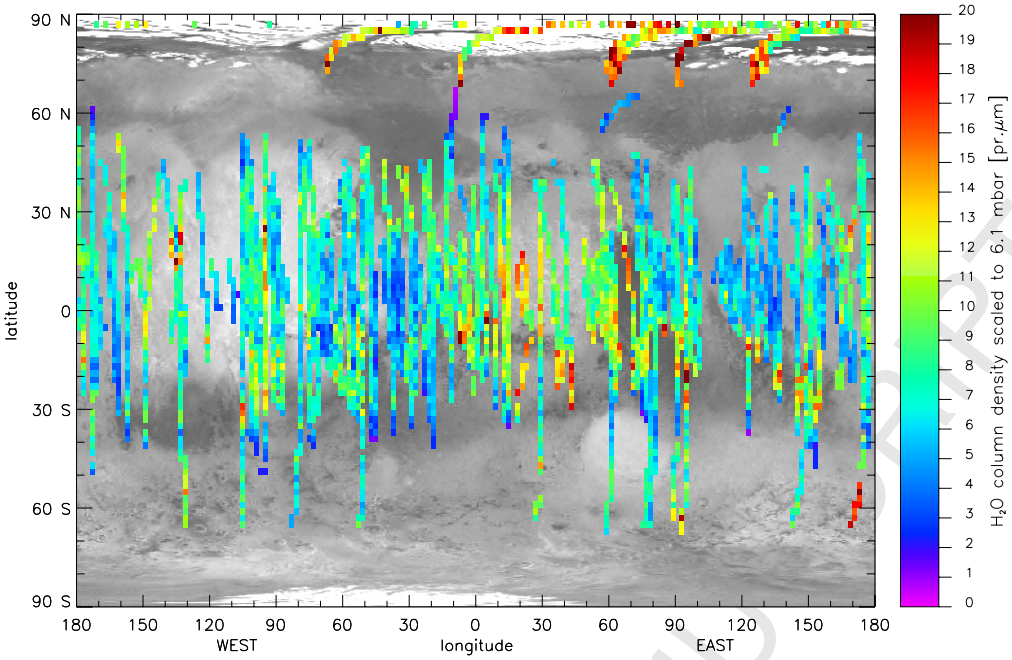

Fig. 9.

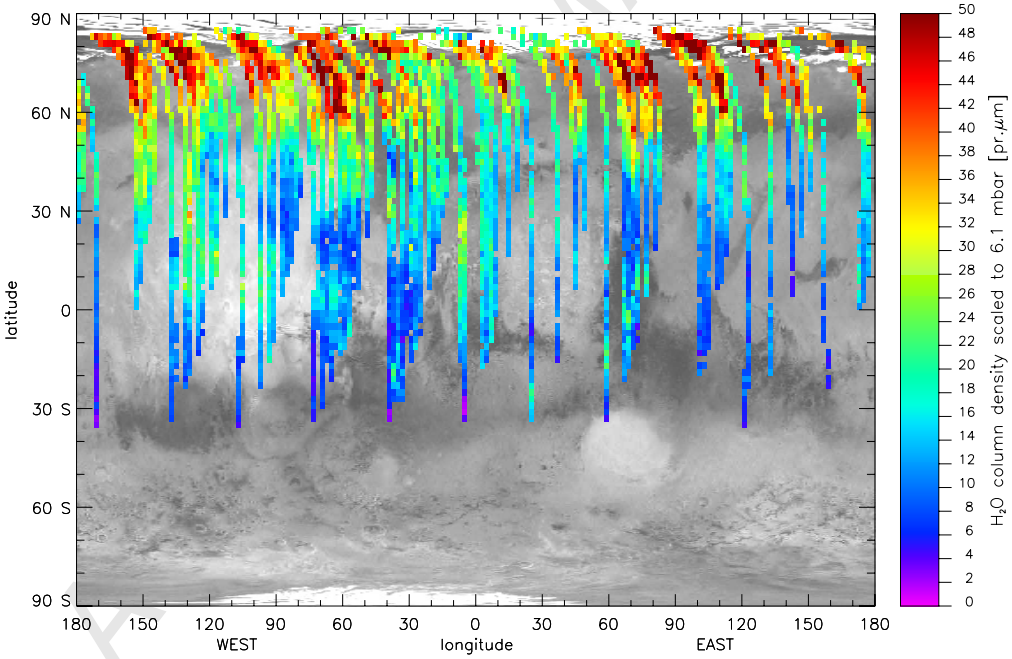

Fig. 10.

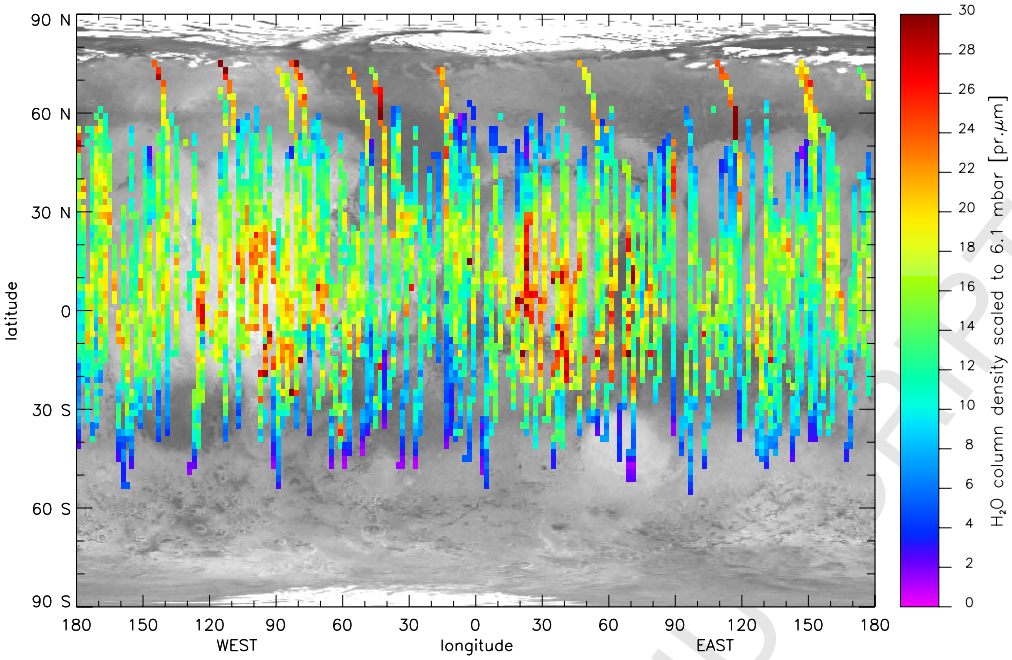

Fig. 11.

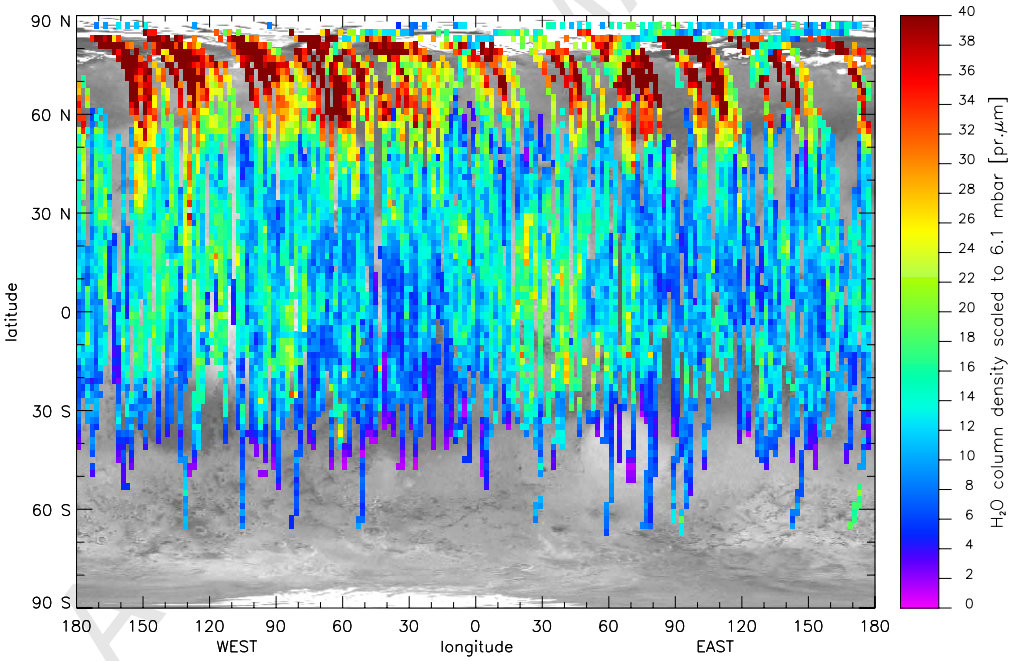

Fig. 12.

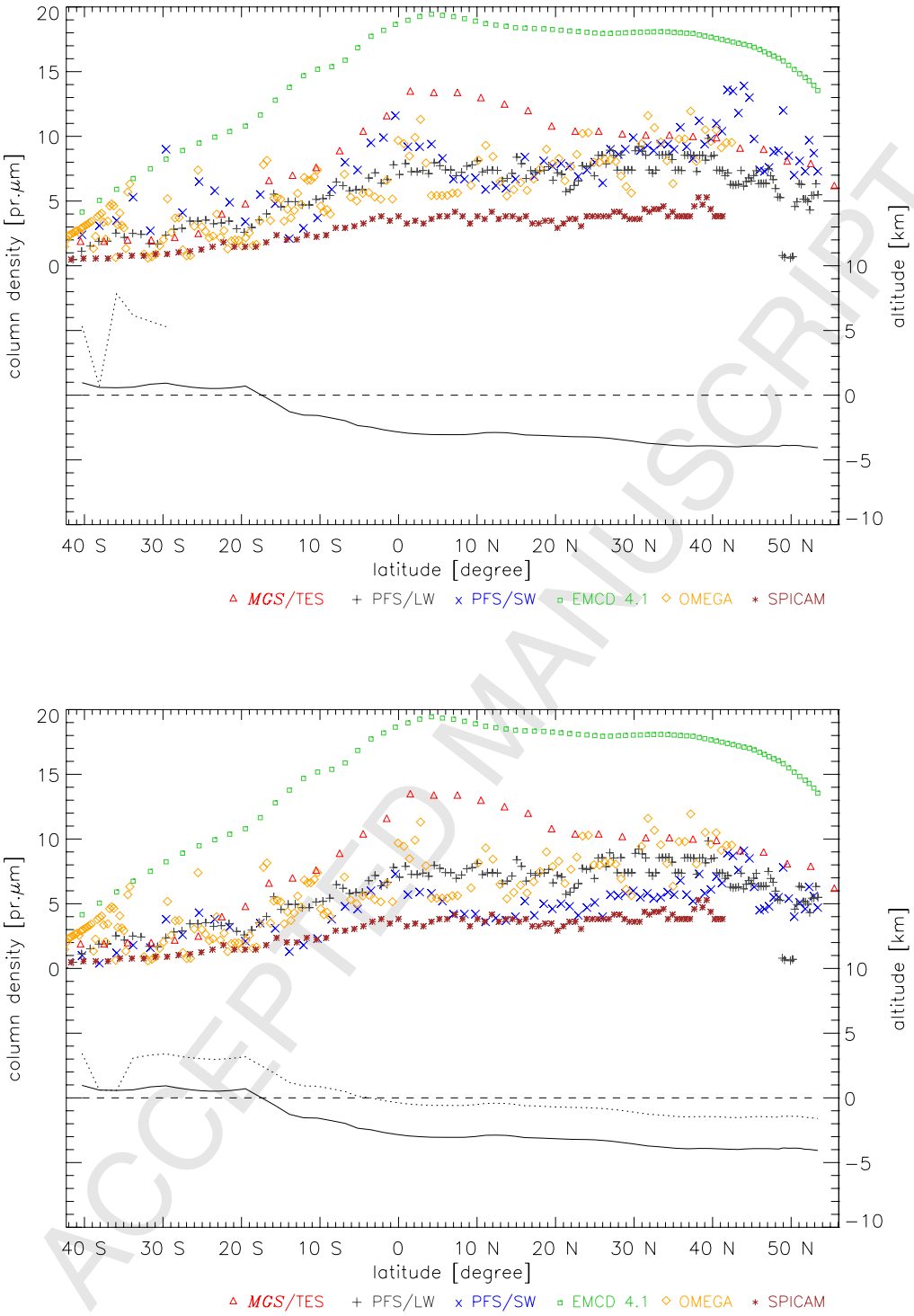

Fig. 13.

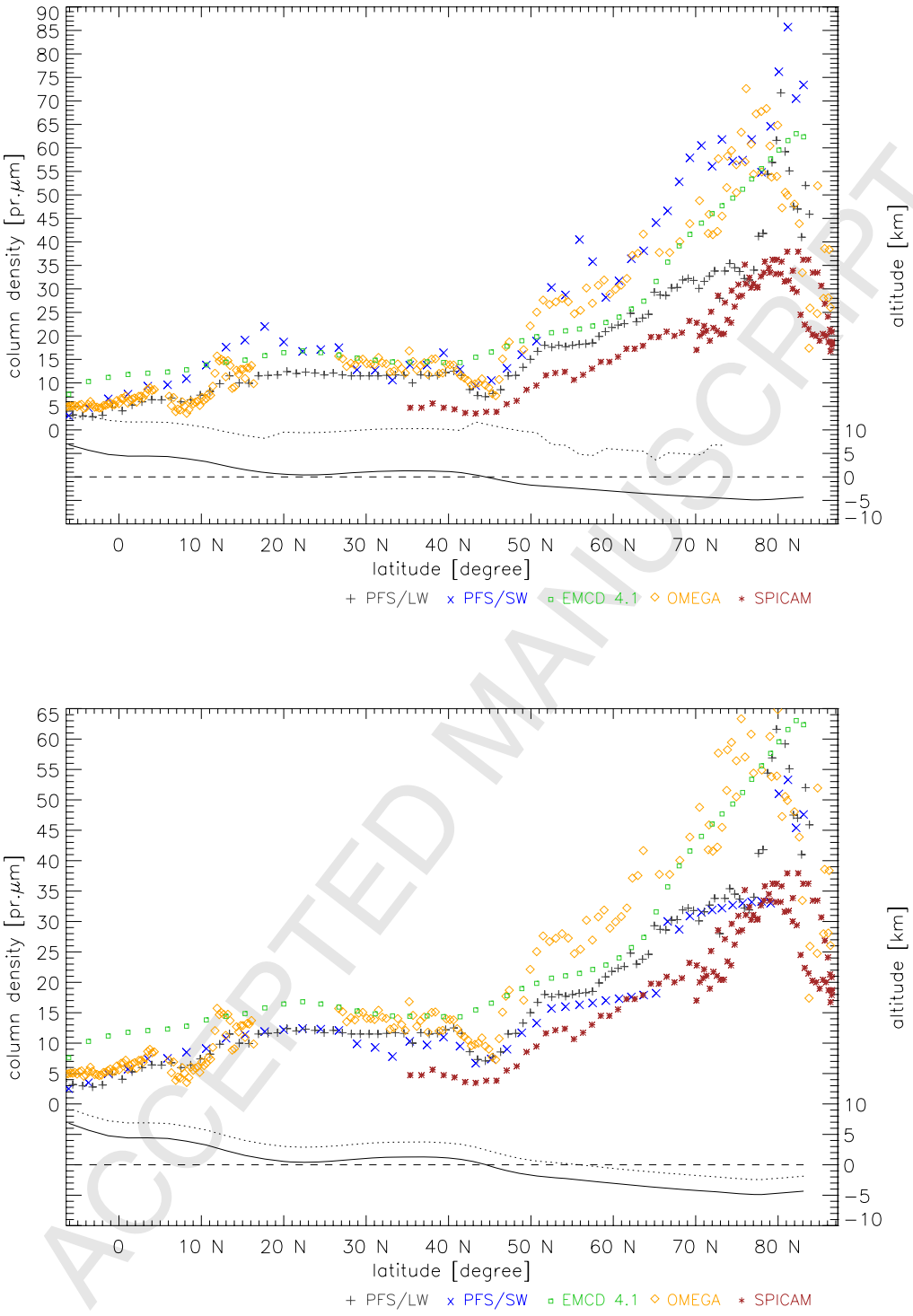

Fig. 14.

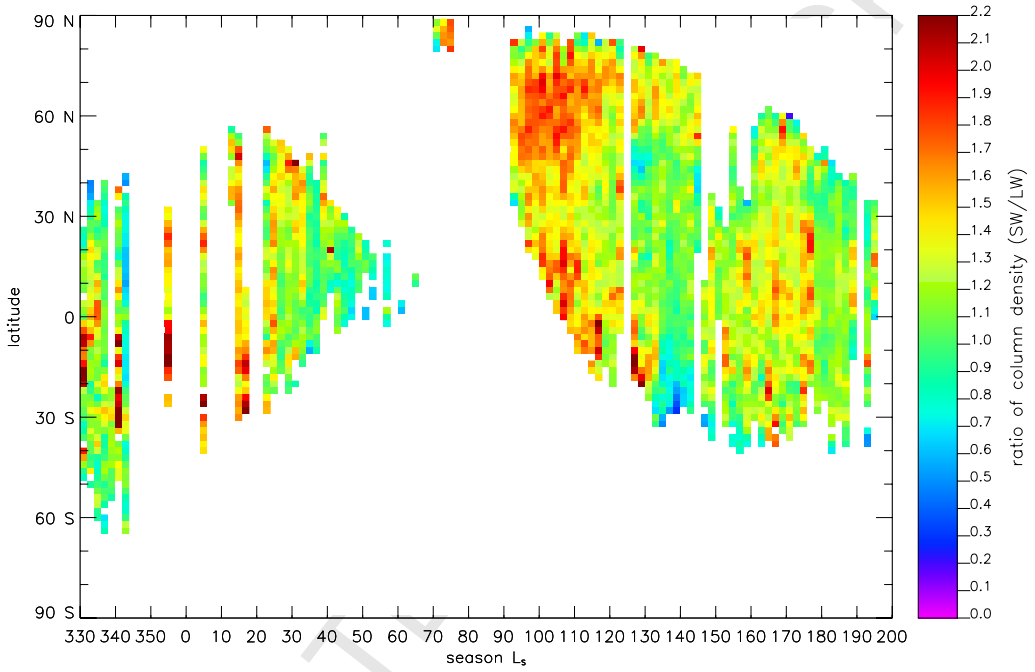

Fig. 15.